Evaluation of Semi-Implicit and Explicit Sedimentation Approaches in the Two-Moment Cloud Microphysics Scheme of ICON

Simon Bolt[1] and Nadja Omanovic[1]

[1]Institute for Atmospheric and Climate Science, ETH Zurich, Zurich, Switzerland

Correspondence: Nadja Omanovic (nadja.omanovic@env.ethz.ch)

Abstract. In the ICOsahedral Nonhydrostatic (ICON) model, the Seifert-Beheng two-moment microphysics scheme is one approach to simulate clouds with different hydrometeor classes. In this bulk description, sedimentation is modeled by advecting the first two moments (number and mass densities) of the hydrometeor size distributions with velocities derived from fitting a generalized gamma distribution to the moments. This method implicitly relies on the diffusive properties of the numerical advection schemes to obtain results in closer agreement with the exact spectral solution. The implementation in ICON offers both a semi-implicit and largely untested explicit method for sedimentation. Currently, the semi-implicit scheme is substantially slower on graphics processing units (GPUs), which is particularly relevant considering the recent rise of GPUs in supercomputing; this raises the question of whether the explicit scheme is a viable alternative.

We provide a detailed examination of both sedimentation schemes, their differences, and underlying assumptions. Using idealized one-dimensional experiments, we identify a minor issue in the default semi-implicit scheme (flux limiter artifacts) and propose a solution. Additionally, we show that the explicit scheme exhibits less numerical diffusion, though some diffusion is crucial for accurate bulk sedimentation. We caution that in the future, finer grid resolutions may result in insufficient diffusion, especially for the explicit scheme. An analysis of six case studies with thunderstorms reveals that the explicit scheme gives rise to more jagged patterns in the hydrometeor profiles, although without concerning instabilities. Furthermore, some differences in hail and graupel precipitation rates can be attributed to different ways of considering the microphysical source terms (e.g., hydrometeor interactions) during the sedimentation step.

1 Introduction

Over the past two decades, a tremendous increase in computational power enabled many advances in numerical weather and climate models. Higher resolution in vertical and horizontal dimensions allows explicitly resolving deep convection, significantly improving precipitation forecasts (Lean et al., 2008; Kendon et al., 2014; Ban et al., 2015). Ensemble simulations enable probabilistic assessments (Bauer et al., 2015), and more sophisticated and thus expensive parameterizations such as multi-moment cloud microphysics can be used.

Particularly the rise of graphics processing units (GPUs) in supercomputing benefits weather and climate models due to higher memory bandwidths compared to traditional central processing units (CPUs), and the simulations' largely parallel nature (Owens et al., 2008; Leutwyler et al., 2016). However, enabling a sophisticated atmospheric model to execute well on both

CPUs and GPUs from different generations and hardware manufacturers is very challenging, especially since a single source code with "high usability (...) by non-expert programmers" is strongly desirable due to typically "large developer, and even larger user communities" (Fuhrer et al., 2014). For GPU simulations with the Consortium for Small-Scale Modeling (COSMO) model, Fuhrer et al. (2018) have completely rewritten the dynamical core while porting the physical parameterizations with compiler directives. For the latter, they note, refactoring to recompute variables previously stored in memory played a crucial part, since floating point operations are much cheaper than data movement on modern architectures.

A similar approach with compiler directives was chosen for the ICOsahedral Nonhydrostatic (ICON) model (Zängl et al., 2015), where ETH Zurich, the Center for Climate Systems Modeling (C2SM), and the Swiss Federal Institute of Meteorology and Climatology (MeteoSwiss) had to invest significant resources to port ICON to GPUs for scientific research and operational weather forecasts (Project ICON-22, 2025) using the new Alps computing infrastructure[1] at the Swiss National Supercomputing Centre (CSCS). Still, significant challenges with code maintainability, adaptation to new architectures, and fragile workflows suggest that this approach is unsustainable in the long-term (Paredes et al., 2023).

During this combined effort, it was discovered that one specific physical parameterization, the two-moment cloud microphysics module (Seifert and Beheng, 2006) with some modifications (Segal and Khain, 2006; Blahak, 2008; Seifert, 2008; Noppel et al., 2010), performs particularly slowly on GPUs without significant refactoring. This microphysics scheme is commonly used in a variety of scientific studies, but also operationally by the German Meteorological Service (DWD) in the ICON-RUC (Rapid Update Cycle) model setup (Reinert et al., 2025) since 2024, and MeteoSwiss also considers employing it in the future. For sedimentation, which is part of the microphysics, ICON's default configuration utilizes a semi-implicit advection method based on a Crank-Nicolson discretization that also incorporates the remaining microphysical processes (source terms) with a predictor-corrector method. An alternative but largely untested explicit semi-Lagrangian method is also implemented, employing simple sequential operator splitting for sedimentation and the source terms. Such coupling may be less accurate, as hydrometeor interactions with thin cloud layers could be entirely missed for large sedimentation velocities. However, this explicit variant performs much better on GPUs, shown by runtime measurements in Table 1.

In the future, the resolution of weather and climate models can be expected to further increase, as it improves the representation of clouds and convection (Miyamoto et al., 2013; Heinze et al., 2017; Stevens et al., 2020; Omanovic et al., 2024), and terrain-induced circulations (Schmidli et al., 2018; Heim et al., 2020; Mikkola et al., 2023), in addition to reducing the numerical discretization and coupling errors. Conversely, the two-moment bulk sedimentation description benefits from some numerical diffusion errors to suppress unphysical shockwaves introduced by the parameterization (Wacker and Seifert, 2001), and thus diffusive errors may also be relied upon for stability of the sedimentation schemes.

In light of those aspects, this paper aims to investigate whether or to what extent the explicit sedimentation scheme is a viable alternative to the semi-implicit variant. Currently, the semi-implicit sedimentation scheme is only documented for its initial implementation in the COSMO one-moment scheme (Doms et al., 2021, Sect. 5.2.4), which does not cover several modifications made for use in ICON's two-moment microphysics. Thus, we first provide a concise overview of both sedimentation methods in Sect. 2, without neglecting small but ultimately important implementation details. Using insights from those

---

[1]https://www.cscs.ch/computers/alps, accessed 07 May 2025

Table 1. Runtimes using the two-moment sedimentation scheme as implemented in ICON version 2024.10. We report the two-moment microphysics (total average across processes) and total simulation (in brackets) runtime in seconds, as measured by ICON's built-in timing routines. The runtime for three identical simulations and their mean is shown, using the setup from Sect. 4, except for disabled output. We use a single Grace-Hopper node, consisting of four NVIDIA GH200 superchips, of the Alps supercomputer.

	Semi-implicit		Explicit	
		189 (1390)		170 (1337)
CPU[a]	189 (1369)	188 (1366)	170 (1345)	171 (1353)
		189 (1352)		170 (1344)
		1490 (2080)		77 (660)
GPU[b]	1493 (2084)	1494 (2083)	77 (656)	77 (653)
		1493 (2089)		77 (655)

[a]Total $4 \cdot 72 = 288$ processes, 286 for CPU computation, 1 for I/O, 1 for prefetching

[b]Total 5 processes, 4 for GPU computation, 1 for prefetching

60 numerical descriptions, single-column experiments with pure sedimentation (Sect. 3), and case studies based on full ICON simulations (Sect. 4), we investigate and evaluate the impact of switching between the semi-implicit and explicit schemes, and further configuration options. In the conclusions (Sect. 5), we summarize our findings and give recommendations for future model setups.

2 Sedimentation Schemes in ICON

65 2.1 Sedimentation Description

We start by providing a brief overview of ICON's two-moment microphysics sedimentation description, closely following Wacker and Seifert (2001) and Seifert and Beheng (2006). In general, the hydrometeors are categorized into different classes, namely cloud droplets, rain, cloud ice, snow, graupel, and hail. Each hydrometeor class is modeled by a distinct size distribution with two free parameters, determined by the local number and mass density, i.e., the first two moments of this distribution. 70 Thus, the two-moment description's aim is to describe all microphysical processes, including sedimentation, in terms of those two moments.

The starting point for sedimentation is the one-dimensional spectral budget equation for the number density size distribution f, modeling the pure sedimentation process in vertical direction for different hydrometeors.

$$\frac{\partial}{\partial t} f(z,t,x) = -\frac{\partial}{\partial z} [v(\rho,x) \cdot f(z,t,x)] \tag{1}$$

75 Specifically, $\int_{x_1}^{x_2} f(z,t,x)\,dx$ describes the number density of particles with mass x between x_1 and x_2, and $v(\rho,x) \leq 0$ is the sedimentation velocity depending on particle mass x and atmospheric density ρ. Sources and sinks, e.g., hydrometeor interactions, will be introduced later in Eq. (9). Other processes such as wind-driven advection, turbulent diffusion and saturation

adjustment are treated outside ICON's microphysics module in a time-split manner (Reinert et al., 2024). The moment budget equations arise from integrating Eq. (1) over the mass x. After defining the m-th moment M_m and its sedimentation velocity $\overline{v}_m$,

$$M_m = \int_0^\infty f(z,t,x) \cdot x^m \, dx \tag{2}$$

$$\overline{v}_m = \frac{\int_0^\infty v(\rho,x) \cdot f(z,t,x) \cdot x^m \, dx}{M_m}, \tag{3}$$

an advection equation for each moment M_m is obtained:

$$\frac{\partial}{\partial t} M_m = -\frac{\partial}{\partial z} \left[\overline{v}_m \cdot M_m \right] \tag{4}$$

However, evaluating $\overline{v}_m$ still requires knowledge about the entire size distribution $f(z,t,x)$, rather than just the moments M_0 and M_1. To address this, f is approximated by fitting a generalized Γ-distribution to the moments:

$$f(x) \approx g(x) := A x^\nu \exp\left(-\lambda x^\mu\right) \tag{5}$$

In the case of ice phase hydrometeors (ice crystals, snow, graupel, hail), ν and μ are fixed dimensionless shape parameters, whereas A and λ are to be determined by the two moments. For rain, μ can optionally be further parametrized by a relation to the raindrop diameter (Seifert, 2008). After defining a parameterized relation between the particle mass x and sedimentation speed, e.g., a power law for ice phase hydrometeors, combined with a scaling factor $(\rho_0/\rho)^\gamma$ to account for the increasing atmospheric density ρ, it is possible to evaluate the speed of the m-th moment of the Γ-distribution $g(x)$. Writing $N := M_0$ and $L := M_1$ for the number and mass densities, respectively, we obtain:

$$v_{\text{frozen}}(x) \approx -\alpha x^\beta \left(\frac{\rho_0}{\rho}\right)^\gamma, \tag{6}$$

$$v_m(N,L) = \frac{\int_0^\infty v_{\text{frozen}}(x) \, x^m g(x) \, dx}{M_m} = -c_m \cdot \left(\frac{L}{N}\right)^\beta \cdot \left(\frac{\rho_0}{\rho}\right)^\gamma \tag{7}$$

$$c_m := \alpha \, \frac{\Gamma\left(\frac{m+\nu+\beta+1}{\mu}\right)}{\Gamma\left(\frac{m+\nu+1}{\mu}\right)} \left[\frac{\Gamma\left(\frac{\nu+1}{\mu}\right)}{\Gamma\left(\frac{\nu+2}{\mu}\right)}\right]^\beta \tag{8}$$

For rain, the same procedure is applied to compute the approximate velocities of the moments, but instead of a power law as in Eq. (6), an Atlas-type fall speed relation is used (Seifert et al., 2014).

Finally, when also including the source terms that encompass the remaining microphysical processes, the equation to solve for each hydrometeor class is:

$$\frac{\partial}{\partial t} \begin{bmatrix} N \\ L \end{bmatrix} = -\frac{\partial}{\partial z} \left(\begin{bmatrix} v_0(N,L) \cdot N \\ v_1(N,L) \cdot L \end{bmatrix} \right) + \begin{bmatrix} Q_N(N,L,\dots) \\ Q_L(N,L,\dots) \end{bmatrix} \tag{9}$$

Since the source terms Q_N, Q_L model all hydrometeor interactions including their formation and dissipation, they not only depend on the moments of the current hydrometeor class, but on the entire local atmospheric model state.

It is important to acknowledge the difference to the spectral formulation in Eq. (1). Whereas the spectral description can
be understood as infinitely many linear advection equations, the two-moment bulk description consists of two quasilinear
advection equations, coupled through non-linear velocities (and source terms). This is a fundamentally different structure,
particularly, only the bulk description leads to the emergence of unrealistic shock waves (Wacker and Seifert, 2001). In practice,
this can mostly be compensated by the deliberate use of diffusive numerical schemes for solving Eq. (9).

2.2 Semi-Implicit Scheme

For clarity and conciseness, we will use ϕ to describe both N and L for all hydrometeor classes, and likewise use the generic
velocity v, referring to the respective moment and class' velocity function. Furthermore, Table 2 provides a brief summary over
both sedimentation schemes, which will be presented in great detail next.

Table 2. Brief overview over the two sedimentation schemes as implemented in ICON version 2025.04.

	Semi-implicit	Explicit
Numerical description	Crank-Nicolson, upwind flux	FFSL, piecewise constant reconstruction
Approximations	Explicit velocities	Straight trajectories without iterations
Source term treatment	Predictor-corrector method (or sequential)	Only sequential
Flux limiter for $\phi \geq 0$	Too restrictive (solution proposed)	Non-restrictive
Stability	Unproblematic in practice[a]	Lipschitz condition
Substepping	Not implemented	Possible
GPU performance	Unacceptably slow[b]	Acceptable

[a]The explicit velocity approximation from Eq. (12) theoretically impacts stability.

[b]In case of predictor-corrector source term treatment, otherwise only slightly slower than the explicit scheme. Table 1 lists runtimes of default
configurations.

The semi-implicit scheme is the default method to solve Eq. (9) in ICON. Originally used in the COSMO one-moment
scheme (Doms et al., 2021), it was adapted and modified for the two-moment microphysics of ICON. It employs a mass-
conserving Crank-Nicolson discretization with upwind flux for the advection terms, and an explicit approximation for velocities
to avoid solving non-linear systems. In the default configuration, source terms are handled by a predictor-corrector method,
which intertwines the sources with sedimentation. The default semi-implicit scheme's update step is given by

$$\phi_k^* = \left(1 - \frac{\Delta t}{2\Delta z_k} \widetilde{v}_k^{(n+1)}\right)^{-1} \cdot \left[\phi_k^{(n)} - \frac{\Delta t}{2\Delta z_k} \left((\widetilde{v}\phi)_{k-1}^{(n+1)} + (v\phi)_{k-1}^{(n),\text{lim}} - (v\phi)_k^{(n),\text{lim}}\right)\right] \tag{10}$$

$$\phi_k^{(n+1)} = \left(1 - \frac{\Delta t}{2\Delta z_k} \widetilde{v}_k^{(n+1)}\right)^{-1} \cdot \left[\phi_k^{(n)} - \frac{\Delta t}{2\Delta z_k} \left((\widetilde{v}\phi)_{k-1}^{(n+1)} + (v\phi)_{k-1}^{(n),\text{lim}} - (v\phi)_k^{(n),\text{lim}}\right) + Q_k\left(\phi_k^*\right)\Delta t\right], \tag{11}$$

where the sub- and superscripts are level and time indices, respectively. Notably, ICON uses a reversed level indexing con-
vention compared to the z-axis direction, i.e., level $k = 1$ is the uppermost level. Furthermore, ρ is assumed constant in time
during a single update step, and writing $v_k^{(n)}$ for $v_m(N_k^{(n)}, L_k^{(n)})$, the implicit velocity $v_k^{(n+1)}$ was replaced by the explicit

approximation

$$\widetilde{v}_k^{(n+1)} := \frac{1}{2}\left(v_k^{(n)} + v_{k-1}^{(n)}\right).$$ (12)

125   This approximation, in combination with the upwind flux, greatly reduces the computational effort since it eliminates the need to solve any (non-linear) systems of equations with iterative methods. Instead, Eq. (11) can simply be applied level by level, i.e., starting from the domain's top at $k = 1$, simultaneously for all hydrometeor classes and moments.

   For physical reasons, mass and number concentrations should also remain nonnegative during the update step. This is achieved, without violating mass conservation, by applying a flux limiter:

130    $$(v\phi)_k^{(n),\mathrm{lim}1} := \max\left\{(v\phi)_k^{(n)}, \ (\widetilde{v}\phi)_{k-1}^{(n+1)} + (v\phi)_{k-1}^{(n),\mathrm{lim}1}\right\}.$$ (13)

This limiter enforces that the square bracket in Eq. (10) remains $\geq \phi_k^{(n)}$, and thus $\phi_k^* \geq 0$ as well. However, this limiter is ultimately arbitrary and too restrictive, since it does not consider the effect of time integration. Hence, we propose an improved flux limiter, which only activates when $\phi < 0$ would emerge during time integration. In other words, we should only enforce that the square bracket in Eq. (10) remains ≥ 0, as opposed to $\geq \phi_k^{(n)}$:

135    $$(v\phi)_k^{(n),\mathrm{lim}2} := \max\left\{(v\phi)_k^{(n)}, \ (\widetilde{v}\phi)_{k-1}^{(n+1)} + (v\phi)_{k-1}^{(n),\mathrm{lim}2} - \frac{2\Delta z_k}{\Delta t}\phi_k^{(n)}\right\}.$$ (14)

Notably, both flux limiter versions are also sufficient to guarantee $\phi_k^{(n+1)} \geq 0$ when used in Eq. (11) where the sources are applied, since ICON's source term computation also guarantees $\phi_k^* + Q_k(\phi_k^*)\Delta t \geq 0$.

   Instead of the predictor-corrector method described by Eqs. (10) and (11), it is also possible to treat the source terms with sequential operator splitting, i.e., by simply integrating the source terms before applying the sedimentation step:

140    $$\phi^{(n)} \leftarrow \phi^{(n)} + Q\left(\phi^{(n)}\right)\Delta t$$ (15)

$$\phi_k^{(n+1)} = \left(1 - \frac{\Delta t}{2\Delta z_k}\widetilde{v}_k^{(n+1)}\right)^{-1} \cdot \left[\phi_k^{(n)} - \frac{\Delta t}{2\Delta z_k}\left((\widetilde{v}\phi)_{k-1}^{(n+1)} + (v\phi)_{k-1}^{(n),\mathrm{lim}} - (v\phi)_k^{(n),\mathrm{lim}}\right)\right].$$ (16)

In this variant, the source terms are computed in the entire domain at once, as opposed to the level-wise calculation required in the predictor-corrector configuration. In fact, this would improve the semi-implicit scheme's GPU performance significantly, but makes virtually no difference for CPUs: Currently, the source term computation has very high overhead on GPUs due to a large number of GPU kernel launches. Since this overhead remains fixed regardless of the computational domain's size,

145   the combined overhead of the level-wise calculation exceeds that of the all-at-once approach by a factor equal to the number of levels. This accounts for nearly all the runtime differences between the default semi-implicit and explicit sedimentation schemes as shown in Table 1, since the explicit scheme only offers the sequential source term treatment (see Sect. 2.3).

2.3   Explicit Scheme

150   The explicit scheme for hydrometeor sedimentation is a rather simple, conservative first order flux-form semi-Lagrangian (FFSL) method using straight-line trajectories and a piecewise constant reconstruction (Blahak, 2020). Furthermore, sedimentation and source terms are treated with operator splitting, i.e., simply applied sequentially, analogous to Eqs. (15) and (16) for

the semi-implicit scheme. The explicit method's update step is described by

$$\phi^{(n)} \leftarrow \phi^{(n)} + Q\left(\phi^{(n)}\right)\Delta t \tag{17}$$

$$155 \quad \phi_k^{(n+1)} = \phi_k^{(n)} - \frac{\Delta t}{\Delta z_k}\left(\overline{P}_{k-\frac{1}{2}}^{\text{lim}} - \overline{P}_{k+\frac{1}{2}}^{\text{lim}}\right), \tag{18}$$

where the time-averaged fluxes $\overline{P}$ are approximated by

$$\overline{P}_{k+\frac{1}{2}} \approx -\frac{1}{\Delta t}\sum_{l=0}^{k-1}\phi_{k-l}\cdot(z_{\text{up}} - z_{\text{low}}) \tag{19}$$

$$z_{\text{up}} = \min\left[z_{k+\frac{1}{2}-l-1},\ z_{k+\frac{1}{2}} + |v_{k-l}|\Delta t\right],\ z_{\text{low}} = \min\left[z_{k+\frac{1}{2}-l},\ z_{\text{up}}\right] \tag{20}$$

with the flux limiter

$$160 \quad \overline{P}_{k+\frac{1}{2}}^{\text{lim}} := \max\left[\overline{P}_{k+\frac{1}{2}},\ \overline{P}_{k-\frac{1}{2}}^{\text{lim}} - \phi_k^{(n)}\frac{\Delta z_k}{\Delta t}\right]. \tag{21}$$

This flux limiter simply ensures $\phi_k^{(n+1)} \geq 0$, which can easily be seen from inserting Eq. (21) into (18), while also conserving mass. A geometric interpretation for the flux computation in Eq. (19) is helpful, illustrated by Fig. 1. For each cell $k-l$, a linear trajectory with slope $1/v_{k-l}^{(n)}$ is assumed, i.e., the cell is notionally moved by the distance $v_{k-l}^{(n)}\Delta t$ to obtain its arrival region. Then, $z_{\text{up}} - z_{\text{low}}$ simply describes how much of the notionally moved cell has passed by the cell face at location $z_{k+\frac{1}{2}}$, as visualized in Fig. 1. Thus, $\phi_{k-l}\cdot(z_{\text{up}} - z_{\text{low}})$ describes the integrated amount of ϕ_{k-l} that has passed the cell face $z_{k+\frac{1}{2}}$ under the assumption of a cell-wise constant ϕ.

In contrast to typical explicit Eulerian methods, this FFSL scheme is not constrained by the Courant number $C := |v|\Delta t/\Delta z$, however, a different restriction appears. Smolarkiewicz and Pudykiewicz (1992) derive a limitation on the Lipschitz number $\mathcal{B}$ as a trajectory iteration convergence condition:

$$170 \quad \mathcal{B} := \left|\frac{\partial v}{\partial z}\right|\Delta t < 1 \tag{22}$$

This can be interpreted as preventing the trajectories from intersecting, thus controlling "topological issues (connectivity preservation) in computational flows" (Smolarkiewicz and Pudykiewicz, 1992). Although our simple FFSL scheme does not iterate on the trajectories to obtain a higher-order approximation, e.g., as outlined by Staniforth and Côté (1991), this Lipschitz condition remains highly relevant: $\mathcal{B} > 1$ still leads to issues with the flow's connectivity and may thus introduce spurious oscillations, e.g., when fluid particles originally located in adjacent cells end up several cells apart after a single time step, leaving an empty gap in-between.

Usually, the Lipschitz condition is far more lenient than the CFL condition ($C \leq 1$) of typical explicit Eulerian methods (e.g., Skamarock, 2006). In our case however, where the velocity non-linearly depends on N and L, one can imagine a case where $v = 0$ in one cell, and $|v| \gg 0$ adjacently. In other words, the Lipschitz condition may reduce to $\mathcal{B} = |v|\Delta t/\Delta z < 1$ in the worst case, which is similar to the CFL condition. Still, a Lipschitz condition violation does not necessarily lead to severe stability issues, e.g., Smolarkiewicz and Pudykiewicz (1992) only conclude that the numerical solution becomes "meaningless"
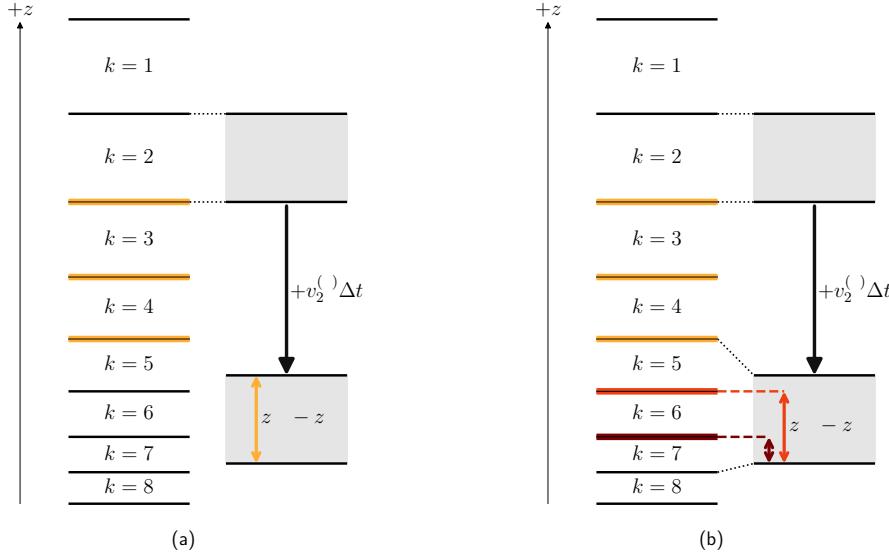
Figure 1. Visualization of the flux computation for the explicit method as described by Eq. (19). The index k, decreasing with height z, denotes levels separated by cell faces (horizontal lines). The contribution of level $k - l = 2$ to all fluxes $\overline{P}_{k+\frac{1}{2}}$ is shown, i.e., when $k - l = 2$ is encountered in the sum in Eq. (19). The cell $k - l = 2$ (shaded gray) is notionally moved along its linear trajectory with slope $1/v_{k-l}^{(n)}$, i.e., displaced by the distance $v_{k-l}^{(n)} \Delta t$ as illustrated by the black arrow. (a) Cell faces at locations $z_{k+\frac{1}{2}}$ for $k \in \{2, 3, 4\}$, highlighted in yellow, are fully traversed by the notionally moved cell. For those cell faces, the flux contribution from level $k - l = 2$ is $\phi_2^{(n)} \Delta z_2 / \Delta t$, i.e., $z_{\text{up}} - z_{\text{low}} = \Delta z_2$ per Eq. (20), as shown by the yellow arrow. As the time integration with Eq. (18) only depends on the flux difference $\overline{P}_{k-\frac{1}{2}} - \overline{P}_{k+\frac{1}{2}}$, the values in levels $k \in \{3, 4\}$ remain unaffected by level $k - l = 2$. (b) Cell faces partially traversed by the notionally moved cell $k - l = 2$, marked by the red and dark red lines, are also considered. Here, the weighting $z_{\text{up}} - z_{\text{low}}$ corresponds to the distance from the moved cell's lower face, shown by the red arrows. Consequently, values from level $k - l = 2$ are distributed to levels $k \in \{5, 6, 7\}$. The extent of numerical diffusion thus depends on how closely the moved cell aligns with the actual cell faces.

for $\mathcal{B} > 1$. For the explicit sedimentation scheme discussed here, we observe that minor vertical oscillations of the mean hydrometeor mass L/N are sometimes introduced in case of $C > 1$, even for $\mathcal{B} \ll 1$, presumably as a combined effect of how the trajectories align with cell faces (see Fig. 1), and the two moments' different sedimentation speed. Since this then leads

185 to velocity variations, such perturbations can further grow and propagate if diffusive processes are unable to provide enough smoothing, until reaching $\mathcal{B} > 1$ as illustrated by Fig. A1. When the Lipschitz condition is violated, we often see the emergence of rapid oscillations, however, such violations may also remain brief and not cause significant effects. If oscillations appear, they do not blow up, thanks to mass conservation and applied mean particle mass bounds, and eventually exit the domain upon reaching the ground. Furthermore, in non-idealized scenarios, smoothing effects caused by tracer advection, turbulent

190 diffusion and the source terms alleviate the problem by reducing the spatial variations of N and L, thus also of v and the Lipschitz number $\mathcal{B}$.

Finally, the explicit scheme also supports so-called sedimentation substepping for the rapidly sedimenting hydrometeor classes (rain, graupel, hail), where the explicit sedimentation update step described by Eq. (18) is simply applied repeatedly, i.e., N_{sub} times with a reduced time step $\Delta t / N_{\mathrm{sub}}$. Importantly, substepping only applies to sedimentation, such that the source term application given in Eq. (17) remains unaffected. Presently, the number of substeps is chosen to keep $C \lesssim 1$ based on an upper bound for hydrometeor velocities $\overline{v}_{\max}$, as used later in Eq. (25):

$$N_{\mathrm{sub}} = \left\lceil \overline{v}_{\max} \, \Delta t / \min_{k}(\Delta z_k) \right\rceil . \tag{23}$$

We should note that $\overline{v}_{\max}$ is enforced prior to scaling with atmospheric density in Eq. (25), such that $C \leq 1$ is not always strictly guaranteed. Further, the minimum of Δz is computed over the local domain, which is determined by partitioning the entire simulation region according to the number of processes. Therefore, $\min_{k}(\Delta z_k)$ might vary slightly across the domain, depending on the domain decomposition. To improve reproducability in full ICON simulations, we manually fix N_{sub} to the highest value encountered across all processes, i.e., across the entire simulation domain.

Clearly, substepping lowers both the Courant and Lipschitz numbers, and should therefore reduce the occurrence rate of Lipschitz condition violations which in turn decreases spurious oscillations at the cost of higher computational cost and more numerical diffusion.

2.4 Number and velocity restrictions

In practice, the bulk sedimentation Eq. (9), with velocities obtained from Eq. (7) comprises some challenges, particularly when N and L are close to or exactly zero. In such cases, the mean mass $\overline{x} = L/N$, and consequently the bulk velocities $v_m(N, L)$, are either extremely sensitive to small changes, or not well-defined at all. Furthermore, $\overline{x}$, and thus $v_m(N, L)$ too, are unbounded, and we must address physical consistency issues like obtaining nonzero mass ($L > 0$) without particles ($N = 0$). Notably, such problematic conditions are mostly observed on the leading edge of a precipitation column, since L sediments faster than N. This is also precisely where excessive size sorting (and consequently spurious reflectivity growth) can be observed, compared to the spectral formulation. Various techniques have been tried to control this issue, e.g., by applying corrections based on the diagnosed reflectivity and/or adjusting distribution shape parameters (Milbrandt and Yau, 2005; Mansell, 2010).

Therefore, the choices made for handling edge cases with small N, L ultimately impact the numerical results quite significantly, and thus we will need provide further implementation details for ICON. First, just before each microphysics step, number concentrations are adjusted to respect lower and upper bounds for the mean particle mass:

$$N \leftarrow \begin{cases} \mathrm{clamp}\left(N, \, \frac{L}{\overline{x}_{\max}}, \, \frac{L}{\overline{x}_{\min}}\right) & \text{if } L > 10^{-12} \, \mathrm{kg\,m^{-3}} \\ 0 & \text{else} \end{cases} \tag{24}$$

Next, the sedimentation velocity computation from Eq. (7) is modified to respect the same mean mass limits, in addition to velocity bounds before scaling with atmospheric density. Also, a threshold q_{crit}, named similarly in ICON's code, is used to

avoid some computations:

$$
v_m(N,L) \approx \begin{cases} -\left(\frac{\rho_0}{\rho}\right)^\gamma \cdot \text{clamp}\left(c_m \cdot \left[\text{clamp}(\frac{L}{N}, \overline{x}_{\min}, \overline{x}_{\max})\right]^\beta, \overline{v}_{\min}, \overline{v}_{\max}\right) & \text{if } L > q_{\text{crit}} := 10^{-9}\,\text{kg}\,\text{m}^{-3} \\ 0 & \text{else} \end{cases} . \tag{25}
$$

In idealized single-column experiments and high Courant numbers in combination with the semi-implicit scheme, such a
threshold q_{crit} may actually prove problematic for the velocity approximation in Eq. (12). At the leading edge of a precipitation
column, where L drops below q_{crit}, this threshold can only propagate by two levels per time step, which results in a strong
shock wave if the actual propagation speed is larger. This could be remedied by either skipping the q_{crit}-based case distinction
in Eq. (25), or using a different approximation for $\widetilde{v}^{(n+1)}$, e.g., $\widetilde{v}_k^{(n+1)} = 0.5 \cdot \left(v_k^{(n)} + v_{k-1}^{(n+1)}\right)$, which incurs slightly higher
computational cost from additionally computing the velocities $v^{(n+1)}$. However, in practice this issue occurs extremely rarely,
as it is almost impossible to uphold those problematic conditions for any significant amount of time, particularly as the three-
dimensional microphysical tracer fields are also mixed and smoothed through tracer advection and the turbulent diffusion
scheme in-between each microphysics step.

Finally, during the source term computation, further constraints are enforced. Writing $\Psi^{\Delta t}$ for the discrete evolution operator
of the combined source terms, i.e., $\Psi^{\Delta t}(\phi) = \phi + Q\Delta t$, the source terms can be separated into four parts:

$$
\Psi^{\Delta t} = \mathcal{X} \circ \mathcal{Q}^{\Delta t} \circ \mathcal{D} \circ \mathcal{Q}_{\text{CCN}} \quad , \text{ with } \quad \mathcal{Q}^{\Delta t} = \cdots \circ \mathcal{Q}_3^{\Delta t} \circ \mathcal{Q}_2^{\Delta t} \circ \mathcal{Q}_1^{\Delta t} \tag{26}
$$

First, $\mathcal{Q}_{\text{CCN}}$ computes the activation of cloud condensation nuclei (CCN), after which the operator $\mathcal{D}$ is applied, dealing with
cases of zero particles with nonzero mass by increasing N. Specifically, if $L > 0$ and $N < 10^{-3}\,\text{m}^{-3}$, the number density
is determined based on assumed particle size distributions, different for each hydrometeor class. Next, the discrete evolution
operator $\mathcal{Q}^{\Delta t}$ represents the actual microphysical interactions, where all processes contained within are again treated with
sequential first order Marchuk-type splitting. Finally, after the microphysical interactions $\mathcal{Q}^{\Delta t}$, the operator $\mathcal{X}$ again enforces
mean particle mass limits by modifying N, exactly as in Eq. (24) but without the case distinction.

3 Idealized Experiments

Next, we will compare and analyze the two sedimentation schemes in an idealized single-column setting and assess their
performance relative to the spectral formulation. As we have pointed out, both methods are deliberately very diffusive (and
thus almost by necessity first-order) to suppress shock-like features not present in the original spectral equation. We will first
compare the diffusive properties in a linear advection case. Since the diffusion error scales with Δz in both methods, we will
then investigate the agreement with the spectral solution for a wide range of vertical mesh resolutions, and also examine the
emergence of several numerical artifacts.

Figure 2 depicts the results from a linear advection test case, showing that the semi-implicit method is significantly more
diffusive than the explicit variant. For the latter, substepping increases numerical diffusion. However, in realistic numerical
weather prediction (NWP) model setups, Δz spans approximately two orders of magnitude, e.g., from $20\,\text{m}$ at the lowest levels
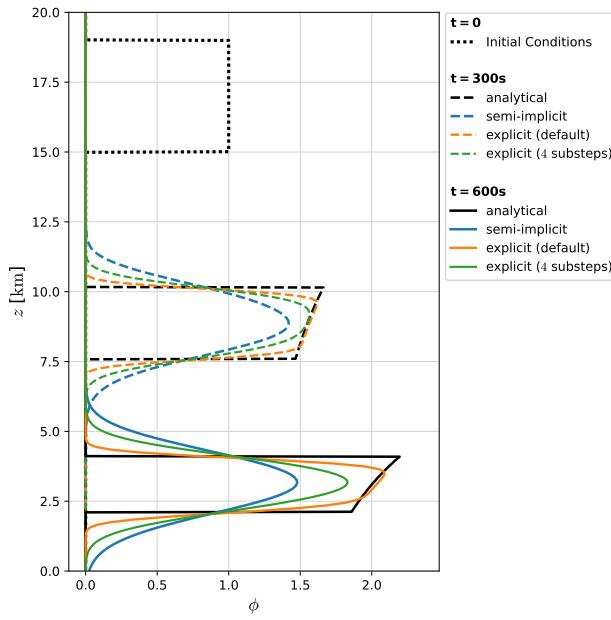
Figure 2. Linear advection, solving $\frac{\partial \phi}{\partial t} = -\frac{\partial}{\partial z}\left(v\left(z\right)\phi\right)$, with $v(z) = -\left(\frac{\rho_0}{\rho(z)}\right)^{\gamma} \cdot 15\,\mathrm{m\,s^{-1}}$, $\rho_0 = 1.225\,\mathrm{kg\,m^{-3}}$, $\gamma = 0.4$, standard atmosphere for $\rho(z)$; with the numerical sedimentation schemes of ICON. The discretization is chosen as $\Delta t = 10\,\mathrm{s}$, $\Delta z = 100\,\mathrm{m}$, thus resulting in the Courant number smoothly increasing from $C = 1.5$ at $z = 0$ to $C = 4$ at $z \approx 19.4\,\mathrm{km}$. Substepping with four substeps is equivalent to a four-fold reduction of Δt (and thus C) in this case.

to over $1\,\mathrm{km}$ at $z \approx 20\,\mathrm{km}$. Considering that, and anticipating future resolution increases in accordance with rising computing power, it is important to understand how the vertical mesh resolution impacts the sedimentation schemes. Figure 3 depicts the setup used to investigate the vertical resolution's impact, showing initial conditions, a spectral reference solution, and

255   hydrometeor profiles for three mesh resolutions and numerical configurations. The agreement between numerical and spectral solutions is evaluated using the standard L^1 norm, and depicted as a function of mesh resolution in Fig. 4.

For the semi-implicit scheme, very high resolution prevents the decay of the structure imposed by the initial conditions, and even generates new extrema. Medium resolutions, roughly of the order $\Delta z \approx 100\,\mathrm{m}$, minimize the discrepancy, although notably, the lowest errors in number and mass densities do not perfectly correspond to the lowest diameter errors. On the

260   contrary, very low resolutions produce overly smooth features, again resulting in large errors. Furthermore, the excessive smoothing also spreads mass to outside the regions where most mass is located in the spectral solution, which would translate to a too early and too late onset and end, respectively, of precipitation on the ground. In those leading and trailing edges of the precipitation column, considerable diameter anomalies can also be observed in Fig. 3.

As the explicit scheme is substantially less diffusive, the mesh resolution that minimizes the discrepancy to the spectral solu-

265   tion is significantly shifted towards coarser resolutions of $\Delta z \approx 500\,\mathrm{m}$ without substepping, whereas the diffusion introduced by substepping results in behavior very comparable to the semi-implicit method.
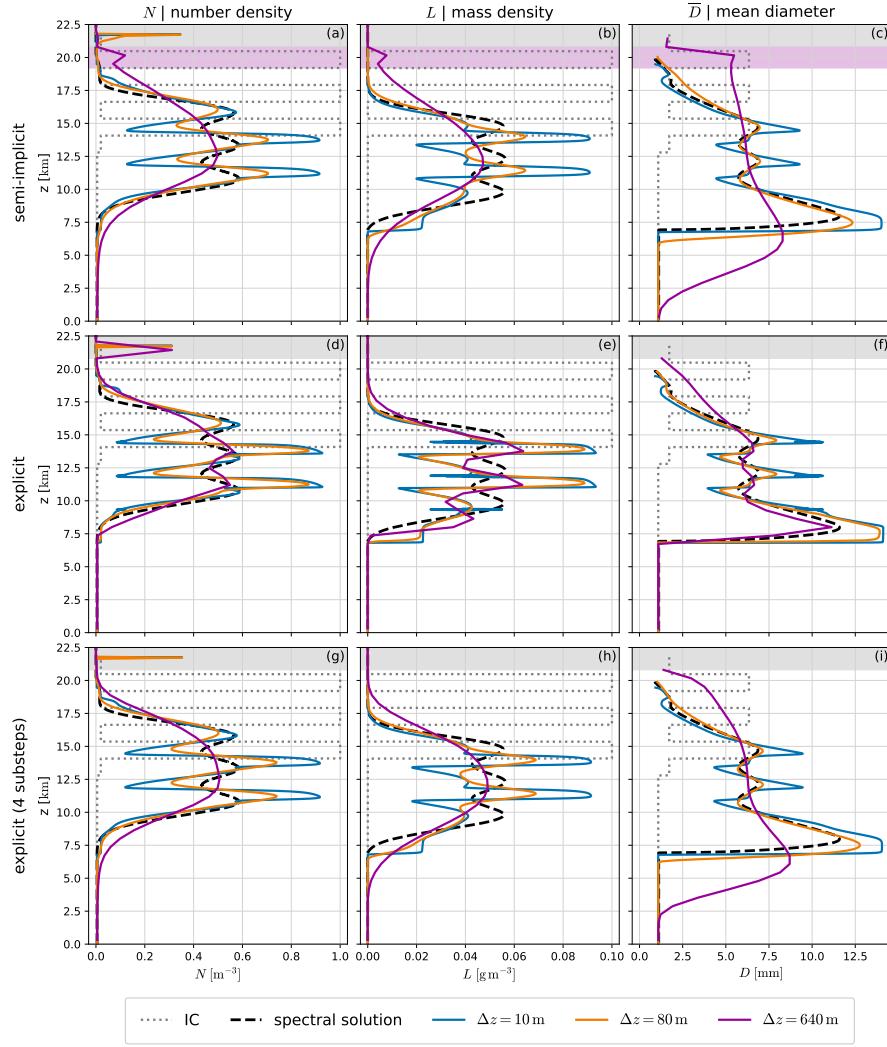
Figure 3. Hydrometeor profiles (N, L, diagnostic mean diameter) in a pure sedimentation case after $t_{end} \approx 534\,s$, for three different mesh resolutions and numerical schemes, in addition to the reference spectral solution. The diameter is only drawn where $L > q_{crit} = 10^{-9}\,\mathrm{kg\,m^{-3}}$. We use the numerical schemes as defined in Sect. 2, except for neglecting all hydrometeor interactions, i.e., $\mathcal{Q}_{CCN}$ and $\mathcal{Q}^{\Delta t}$ from Eq. (26) are skipped. Initial conditions are chosen to be exactly representable on the computational meshes of all resolutions. The time step is selected to be sufficiently small to avoid frequent Lipschitz condition violations (to avoid introducing spurious oscillation in the explicit scheme), and is simultaneously refined with Δz, i.e., $\Delta z / \Delta t = 12\,\mathrm{m\,s^{-1}}$ is held constant. Further, $\rho \equiv \rho_0$ is assumed everywhere, and ICON's hail hydrometeor parameters are used as defined by the constant `graupelhail_cosmo5` in the file `src/atm_phy_schemes/mo_2mom_mcrph_main.f90` of the ICON source code. In the area shaded gray, spikes induced by the operator $\mathcal{D}$, defined in Eq. (26), are visible. The region shaded purple highlights numerical artifacts caused by the flux limiter defined in Eq. (13).
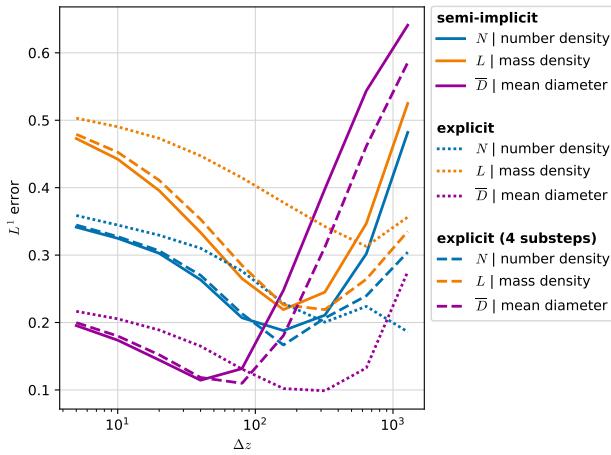
Figure 4. L^1 errors of N, L and diagnostic mean diameter are shown, computed using the numerical schemes in comparison to the spectral solution after a fixed time $t_{\text{end}} \approx 534\,\text{s}$, for spatial resolutions ranging from $\Delta z = 5\,\text{m}$ to $\Delta z = 1280\,\text{m}$ in 2x increments. For the mean diameter, only cells where $L > 10^{-9}\,\text{kg}\,\text{m}^{-3}$ in both spectral and numerical solutions are considered. Initial conditions, profiles at t_{end} for some spatial resolutions, the reference spectral solution, and further setup details are provided by Fig. 3.

In some configurations, the profiles depicted in Fig. 3 exhibit unexpected spikes in the upper domain region, as indicated by the shaded areas. For the number density, the spikes that are shaded gray, arise from the source term's operator $\mathcal{D}$, as defined in Eq. (26). This operator determines the number density based on an assumed particle size distribution when it drops below a threshold. In the configuration shown in Fig. 3 with hail, this is an exponential distribution with respect to the diameter, leading to a sharp increase of N. However, in the semi-implicit scheme, the mass density also displays a spike in the upper domain region, clearly visible in the case $\Delta z = 640\,\text{m}$ in the region highlighted in purple. We can conclusively identify the semi-implicit scheme's restrictive flux limiter, cf. Eq. (13), as the culprit; and here, the effect is further enhanced by the explicit velocity approximation from Eq. (12) which also reduces the sedimentation speed at the highest level where $L > q_{\text{crit}}$ due to the velocity cutoff by q_{crit} in Eq. (25). Additionally, in the locations where those flux limiter artifacts show, even an increase of the mean diameter with height can be observed, which is clearly unphysical as size sorting should produce the opposite effect. In the analysis of case studies, which follows next, we will also investigate the presence of those flux limiter artifacts.

4 Case Studies

Finally, the sedimentation schemes will be examined in full ICON simulations of six individual summer days with significant convective activity. We employ a domain encompassing Switzerland, with $1\,\text{km}$ horizontal resolution and 80 vertical levels, ranging from $\Delta z_{80} \approx 20\,\text{m}$ near the ground to $\Delta z_1 \approx 2\,\text{km}$ in the domain's highest level, terminating at $22\,\text{km}$ height, and the main model time step $\Delta t = 10\,\text{s}$. Simulations were performed from 00:00–22:00 UTC of six distinct days with severe thunderstorms, using COSMO analysis states for initial and lateral boundary conditions. For investigating the sedimentation

Table 3. The five sedimentation scheme configurations used in the full ICON simulations. We differentiate between the semi-implicit (IM) and explicit (EX) schemes, predictor-corrector (pc) and sequential (seq) source term treatment, sedimentation substepping (sub) and the flux limiter improvement (lim) from Eq. (14). The default configuration is IM_{pc}, and it is possible to switch to the EX_{seq} version via ICON's namelist parameters. All other configurations currently require small modifications to the source code, such as changing hard-coded switches.

Configuration	Description
IM_{pc}	Semi-implicit with predictor-corrector source terms, cf. Eqs. (10, 11)
IM_{seq}	Semi-implicit with sequential source terms, cf. Eqs. (15, 16)
$IM_{pc,lim}$	Semi-implicit, predictor-corrector, improved flux limiter from Eq. (14)
EX_{seq}[a]	Explicit with sequential source terms, cf. Eqs. (17, 18)
$EX_{seq,sub}$[b]	Explicit, sequential source terms, sedimentation substepping, cf. Eq. (23)

[a]In this configuration, the numerical sedimentation scheme is significantly less diffusive compared to the rest.
[b]The number of substeps N_{sub}, cf. Eq. (23), is 11 (rain), 41 (graupel), and 16 (hail) for our grid.

schemes, we focus on severe precipitation events such as thunderstorms, particularly including graupel and hail. Therefore, we focus on analyzing the time period from 14:00–20:00 UTC, approximately when the highest density of thunderstorms and precipitation is observed (Dai, 2001; Feldmann et al., 2021).

Since the sedimentation schemes mainly differ in the source term treatment (predictor-corrector or sequential) and the extent of numerical diffusion (explicit is much less diffusive), these two differences are investigated separately by comparing both source term methods in the semi-implicit scheme, and varying the amount of numerical diffusion in the explicit scheme by applying substepping. Furthermore, we also try the semi-implicit scheme with our proposed flux limiter improvement given in Eq. (14); all five configurations are summarized in Table 3.

4.1 Precipitation Rate Roughness

Due to the varying amounts of numerical diffusion in the sedimentation schemes, the vertical hydrometeor profiles are expected to vary in smoothness, possibly amplified by instability-like oscillations from Lipschitz condition violations in the explicit scheme. As the downward movement of the three-dimensional hydrometeor fields effectively transforms the vertical structure into a temporal signal on the ground, we will simply investigate the precipitation rates. Specifically, we define the mean precipitation rate roughness $R(t_n)$ at some time t_n as the spatial mean of absolute temporal second derivatives of instantaneous precipitation rates r_i, using a finite difference approximation:

$$R(t_n) := \frac{1}{N_{cells}} \sum_{i=1}^{N_{cells}} \left| \frac{r_i^{(n-1)} - 2r_i^{(n)} + r_i^{(n+1)}}{\Delta t^2} \right| \tag{27}$$

Figure 5 shows this mean roughness for all six cases, split into rain, graupel, and hail classes. In all cases, the mean roughness of both rain and graupel is more than twice as high using the default explicit scheme in comparison to the other configurations; for hail the behavior is similar, just slightly less pronounced. Considering the semi-implicit versions, the roughness seems
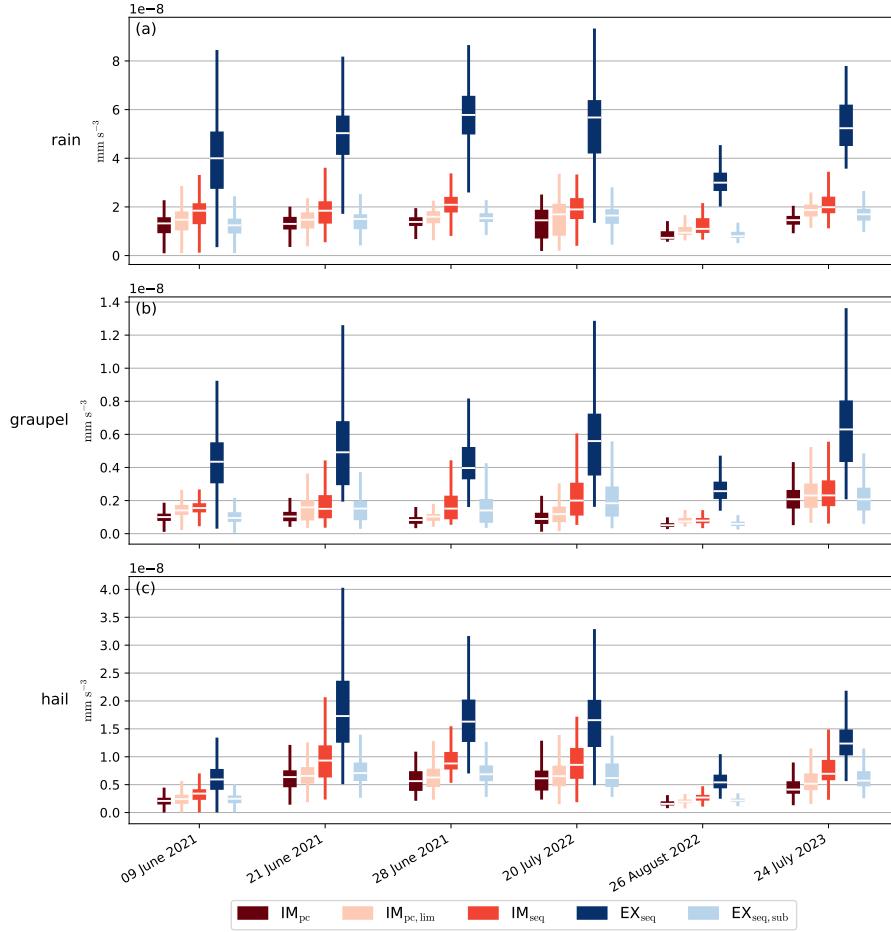
Figure 5. Mean precipitation rate roughness $R(t_n)$ from Eq. (27), over the time period 14:00–20:00 UTC. The corresponding time series are provided by Fig. B1.

to increase very little when switching from predictor-corrector to sequential source term treatment, thus confirming that the large roughness increase of the default explicit scheme is not caused by the source terms. Furthermore, the explicit variant

305 with substepping closely resembles the semi-implicit methods, as expected due to the relaxed Lipschitz condition and more numerical diffusion compared to the default case. Also, the improved flux limiter for the semi-implicit scheme performs very similarly to the default case, possibly with a very slight roughness increase. This would not be surprising, as the improved flux limiter no longer tends to artificially delay (and thus smooth) the trailing edge of precipitation columns, i.e., could allow for more rapid ends of precipitation events.
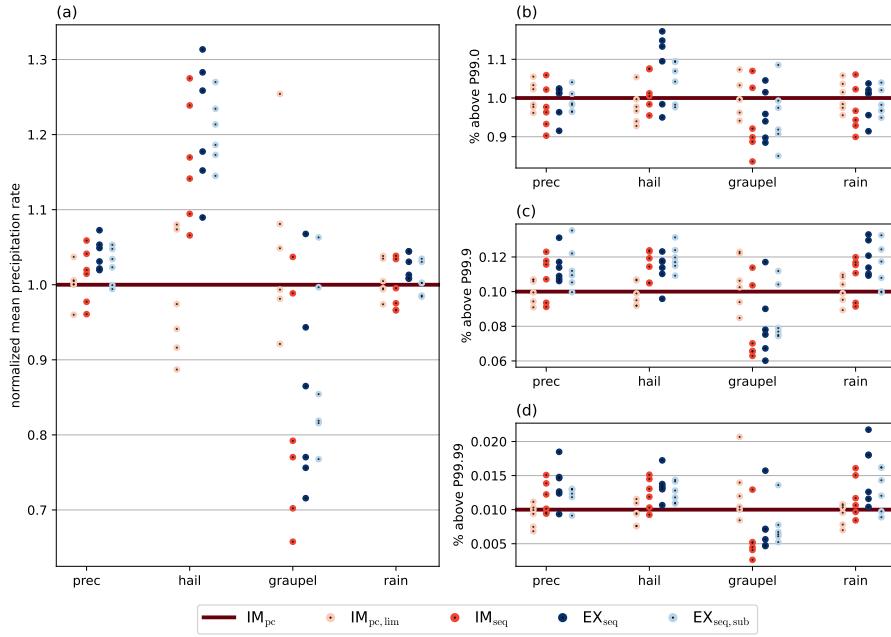
Figure 6. Precipitation rate statistics from 14:00–20:00 UTC for all six cases and the five microphysics configurations from Table 3, using the default semi-implicit scheme as reference. (a) Mean precipitation rates across the space–time domain, normalized by the reference. (b)-(d) How often the (b) 99th, (c) 99.9^{th}, (d) 99.99^{th} percentiles of the reference are exceeded across the space–time domain.

4.2 Precipitation Rate Extrema

If the explicit scheme's less smooth instantaneous precipitation rates were caused by the frequent presence of severe shocks or spurious oscillations, it would be reasonable to expect a correspondingly increased occurrence of extreme precipitation events. Thus, we determine three high percentiles (99th, 99.9^{th}, 99.99^{th}) of the instantaneous precipitation rates in the reference default semi-implicit sedimentation scheme, and then compare how often the other configurations' precipitation rates exceed those thresholds across the domain from 14:00–20:00 UTC, separately for hail, graupel, rain and combined precipitation rates in all six cases.

Figure 6 displays those precipitation rate statistics, in addition to the (relative) mean rates. The default explicit scheme EX_{seq} shows increased mean hail rates in all six cases while reducing the mean graupel rate in five out of six. Interestingly, all other configurations that also apply the source terms sequentially (IM_{seq}, $EX_{seq,sub}$) exhibit the very same behavior, while the $IM_{pc,lim}$ configuration shows no clear deviations from the reference. This clearly indicates that those shifts are caused by the source term treatment as opposed to numerical diffusion differences or spurious oscillations and shocks. For mean rain and combined precipitation rates, all configurations perform relatively similar. Analogous observations can be made for extreme hail and graupel rate events, which occur more and less frequently, respectively, when using the sequential source term treatment. In the 99.9^{th} and 99.99^{th} percentiles, we can further observe slightly higher values in configurations with sequential source

term treatment, while the flux limiter improvement shows no effect again. In summary, all clear trends in the precipitation rate distribution actually result from the different source term treatment rather than instabilities, shocks or reduced numerical diffusion.

Determining why such clear shift from graupel to hail occurs when employing the sequential source term treatment is challenging to explain, especially as there are many pathways to obtain such results. In the sequential treatment, the source terms are integrated with the explicit Euler method, as shown in Eqs. (15) and (17), just before the sedimentation step. Inside the source term computation, the individual microphysical processes are again split sequentially, cf. Eq. (26), also introducing significant splitting errors as discussed by Barrett et al. (2019). Given the fast nature of those microphysical processes, mechanisms creating or growing hail hydrometeors may overshoot, potentially exacerbated by the explicit Euler integration. For example, overshoots in the graupel–hail conversion in wet growth regime would directly lead to the observed effect, especially as no reverse pathway exists because melting does not reduce the hail's bulk density which would warrant such a process (Blahak, 2008). Similarly, the specific ordering of riming processes may amplify hail production, since hail riming is applied before graupel riming.

In contrast, the predictor-corrector treatment integrates source terms within the Crank-Nicolson sedimentation step, as shown in Eq. (11). In this context, the method can be understood as the approximation $0.5 \cdot (Q(\phi_k^{(n)}) + Q(\phi_k^{(n+1)})) \approx Q(\phi_k^*)$ for the time-averaged source term. As ϕ_k^*, given by Eq. (10), already encompasses the source term update of all upstream levels and sedimentation, $Q(\phi_k^*)$ can also be considered a semi-implicit approximation, at least with respect to the upstream levels' contributions. Conversely, in the limit of zero velocity ($v \to 0$), the predictor-corrector and sequential variants are even identical. For fast sedimentation velocities, the share of those implicitly considered contributions thus rises, which may slightly weaken or reduce overshoots of some processes, e.g., the graupel–hail conversion. However, like in the sequential treatment, the individual microphysical processes inside the source term computation are still split sequentially, introducing aforementioned splitting errors. For fast hydrometeors, which repeatedly encounter the source terms (the "implicit contributions") in a single time step, those errors may be smaller or manifest differently compared to the sequential splitting of source terms and sedimentation.

For high sedimentation speeds, particularly $C \gg 1$, the sequential source term treatment suffers from another issue, as it is theoretically possible that some rapidly sedimenting particles fall through thin layers without capturing any interactions, if their positions never actually line up at any time point $t^{(n)}$. Conversely, when positions do line up, interactions may be locally overestimated, since the rapidly falling particles do not actually spend the entire time step in the interaction layer as assumed in the source term computation. Such layer alignment effects may average out or even induce vertical oscillations, depending on the level of diffusion. In contrast, such problems cannot arise with the predictor-corrector method. In practice, however, we are only able to reproduce such missing hydrometeor interactions in idealized experiments with the default explicit scheme, since the extensive numerical diffusion of all other configurations inevitably leads to some interaction. Furthermore, we find that whether a specific process is appropriately captured, or under- or overestimated also heavily depends on its timescale, the sedimentation speed and geometry of the interacting layers, which is also influenced by numerical diffusion. Since many parameters were tuned using the default semi-implicit predictor-corrector configuration for achieving better overall
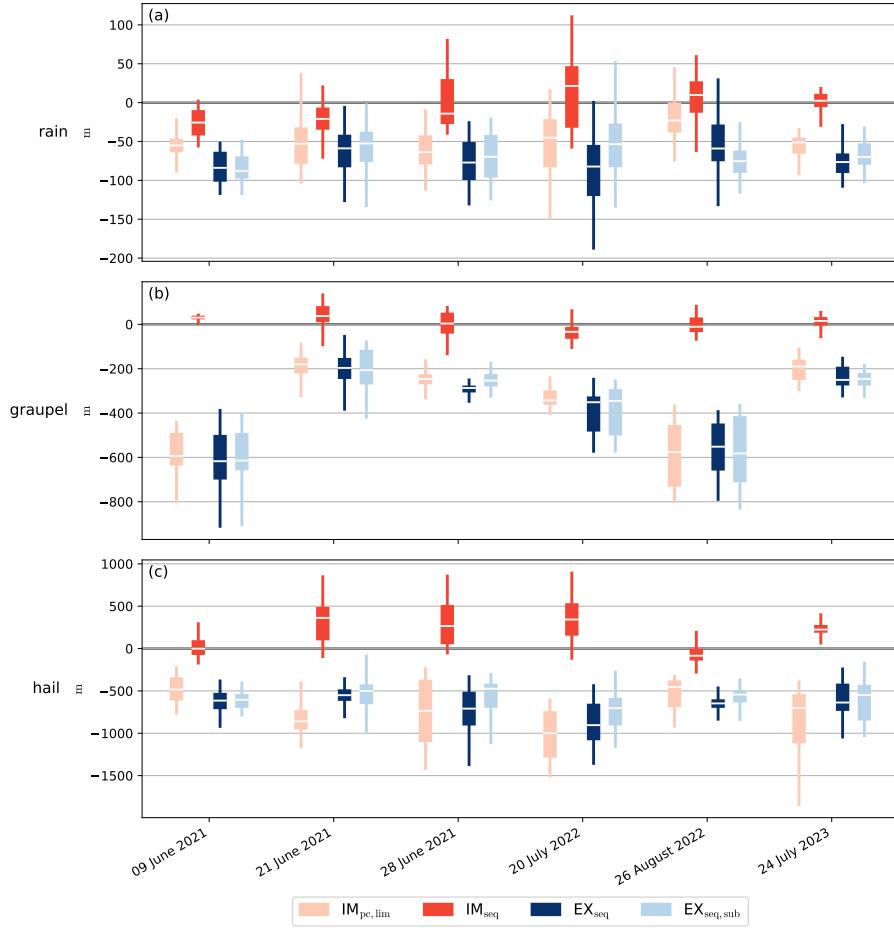
Figure 7. Difference of the mean upper q_{crit} threshold height (i.e., the spatial mean of the highest level's height with $L > q_{\text{crit}} = 10^{-9}\,\text{kg}\,\text{m}^{-3}$, over the columns where such threshold exists), to the default semi-implicit scheme; for the time period 14:00–20:00 UTC with 10 min sampling interval.

skill scores, we suspect those parameters are also inevitably linked to the discretization and splitting errors of this specific model

360 configuration (and resolution), with unclear sensitivities or impacts to changes in the numerical schemes.

4.3 Flux Limiter Artifacts

As we have shown in Sect. 3, the semi-implicit method's current flux limiter is too restrictive, artificially delaying sedimentation of a precipitation column's trailing edge. When used in a two-moment scheme, this even resulted in an unphysical mean diameter increase in those regions, i.e., produced an effect opposite the expected gravitational sorting. Next, we will examine

365 if those flux limiter artifacts translate to the full ICON simulations or turn out to be irrelevant or masked, e.g., by the source terms' operator $\mathcal{D}$ from Eq. (26).

To identify the upper edge of precipitation columns, we make use of the mass density threshold q_{crit}, used in Eq. (25) to determine whether non-negligible mass for sedimentation is present in a cell. In each column, the highest cell with $L > q_{\text{crit}}$ is identified, if it exists, and the mean height of all those cells determined. In Fig. 7, we show the difference of those mean heights

370   compared to the default semi-implicit scheme.

For all three hydrometeor classes (rain, graupel, hail), the IM_{seq} configuration shows almost no difference in the q_{crit} threshold height compared to the default semi-implicit version, except for a slight increase for hail in some cases. Such close agreement indicates that the method to integrate the source terms does not considerably impact this threshold's height, and is expected since both configurations make use of the too restrictive flux limiter given in Eq. (13). Next, the $\text{IM}_{\text{pc,lim}}$ configuration

375   results in consistently lower q_{crit} threshold heights, most pronounced for hail and graupel, but also clearly visible for rain. Again, this is expected due to the improved flux limiter, which no longer artificially slows sedimentation on a precipitation columns' trailing edge. Furthermore the $\text{IM}_{\text{pc,lim}}$ variant performs very similarly to both explicit configurations, which do not suffer from an excessively restrictive limiter. This further confirms that the source term method is irrelevant for this metric, and also strongly suggests that the amount of numerical diffusion is irrelevant as well here. Therefore, the improved flux limiter

380   increases similarity between the two sedimentation schemes' behaviors by eliminating a purely numerical artifact.

5   Summary and Conclusions

We provided a concise and detailed description of the numerical methods and their configuration options employed in ICON's two-moment microphysics module. Since the bulk sedimentation description does not fully capture the original spectral sedimentation equation, e.g., it erroneously produces shock waves, those numerical schemes are deliberately chosen to be very

385   diffusive to compensate. Since the numerical diffusion is not parameterized, its amount heavily depends on the vertical resolution and specific scheme in question; particularly we have shown that the semi-implicit sedimentation scheme is more diffusive than the explicit version. In an idealized setup with pure sedimentation, we observed that too much diffusion leads to reduced size sorting, whereas too little diffusion produces excessive size sorting and reduces the capacity to eliminate the spurious shocks introduced by the bulk velocity approximations.

390   The standard semi-implicit sedimentation scheme is coupled to the microphysical source terms with a predictor-corrector method, resulting in a partially implicit integration of the source terms which is very time-consuming on GPUs in its current form. Moreover, we never encountered any stability issues despite an explicit approximation for some velocities, which works almost surprisingly well. However, we discovered and proposed a solution to a purely numerical artifact caused by a too restrictive flux limiter, leading to artificially delayed sedimentation (and inconsistent size sorting) in trailing edges of hydrometeor

395   columns. In contrast, the explicit scheme employs a simple sequential time-splitting for coupling to the source terms, which are just explicitly integrated before the sedimentation step. For hydrometeors with high sedimentation speeds, the splitting and discretization errors differ compared to the predictor-corrector method, although exact details vary depending on many factors such as the timescale of individual processes, sedimentation speeds, the geometry of interacting layers, and numerical diffusion.

400   In case studies, we have observed significantly rougher instantaneous precipitation rates for the explicit scheme, which directly translates to more jagged patterns in the three-dimensional hydrometeor profiles, likely caused by a combination of factors (reduced numerical diffusion, Lipschitz condition violations). Conversely, changes in the precipitation rate distribution, particularly a shift from graupel to hail, are induced by the different source term treatment. Although in idealized experiments with pure sedimentation, stability of the explicit scheme seems rather fragile in certain cases (oscillations may even appear

405   without violating the Lipschitz condition using high vertical resolutions, and rarely vanish unless they reach the ground), in full model simulations those issues seem to be mitigated by additional diffusive or smoothing operations (turbulent diffusion, tracer advection, source terms). Also, the most problematic high vertical resolutions are only encountered in the lowest levels, which reduces the available time for serious oscillations to develop.

        In the future, NWP model resolutions are likely to increase in accordance with available computing power. This inevitably

410   results in reduced numerical diffusion, which may become problematic for the explicit scheme due to the reduced smoothing capacity for oscillations that are either induced numerically or by the bulk parameterization. Sedimentation substepping, using just a small number of substeps, could serve as effective means to increase the explicit scheme's viability in those cases. In contrast, we do not anticipate comparable issues for the semi-implicit scheme. Given that parameter tuning of the source terms was conducted using the semi-implicit method in predictor-corrector configuration, as currently operational at DWD, GPU

415   performance improvements of the semi-implicit scheme would still be welcome to render it feasible for GPUs. Nevertheless, we find that the explicit scheme can be safely used on GPUs currently, and in case more numerical diffusion is desired, applying a few substeps or the semi-implicit configuration with sequential source terms constitute suitable alternatives with only minor performance impacts.

Code and data availability. We used the open-source ICON model code version 2024.10 for our simulations, available at https://doi.org/10.

420   35089/WDCC/IconRelease2024.10 (ICON partnership (MPI-M, DWD, DKRZ, KIT, and C2SM), 2024) or https://icon-model.org. The code modifications to obtain all model configurations are provided in https://git.iac.ethz.ch/sibolt/icon-model/-/tags. Model data are available from Bolt and Omanovic (2025a) (https://doi.org/10.5281/zenodo.15608275), and plotting scripts, including all code for reproducing the single-column sedimentation experiments, can be obtained from Bolt and Omanovic (2025b) (https://doi.org/10.5281/zenodo.15609459).

Appendix A: Additional figures for pure sedimentation
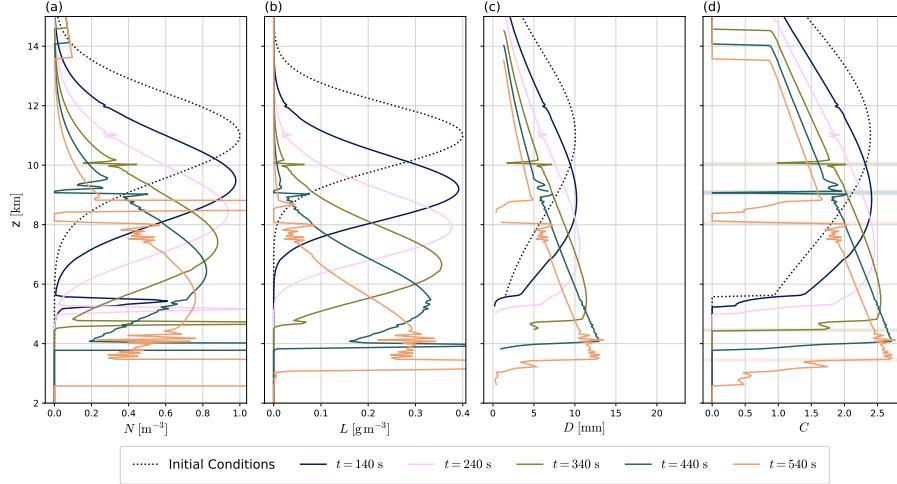
Figure A1. Hydrometeor profiles obtained using the explicit scheme (Sect. 2.3) in a single-column, pure sedimentation configuration, i.e., neglecting $\mathcal{Q}_{\mathrm{CCN}}$ and $\mathcal{Q}^{\Delta t}$ from Eq. (26). We use the vertical resolution $\Delta z = 50\,\mathrm{m}$ with time step $\Delta t = 10\,\mathrm{s}$, $\rho \equiv \rho_0$ is assumed everywhere, and ICON's hail hydrometeor parameters are used as defined by the constant `graupelhail_cosmo5` in the file `src/atm_phy_schemes/mo_2mom_mcrph_main.f90` of the ICON source code. We show the hydrometeor number density (a), mass density (b), and the diagnostic mean diameter (c), drawn where $L > q_{\mathrm{crit}} = 10^{-9}\,\mathrm{kg\,m^{-3}}$. In (d), the mass density's Courant number $C = |v_1(N, L)|\,\Delta t/\Delta z$ is shown, and regions where the Lipschitz condition ($\mathcal{B} < 1$) is violated are marked by the shading in the respective color. In the upper domain region, spurious oscillations slowly develop despite no Lipschitz condition violations, first visible at $t = 140\,\mathrm{s}$, $z = 12\,\mathrm{km}$, and subsequently at $t = 240\,\mathrm{s}$, $z = 11\,\mathrm{km}$. At $t = 340\,\mathrm{s}$, $z = 10\,\mathrm{km}$, $\mathcal{B} > 1$ is reached for the first time, such that oscillations further grow and the originally single-peak profile is split in two ($t = 540\,\mathrm{s}$). Oscillations in the lower domain region are initially induced by the operator $\mathcal{D}$ from Eq. (26), since it sharply increases the number density. In this figure, colors from Crameri et al. (2020) are used.

425 **Appendix B: Additional figures for case studies**
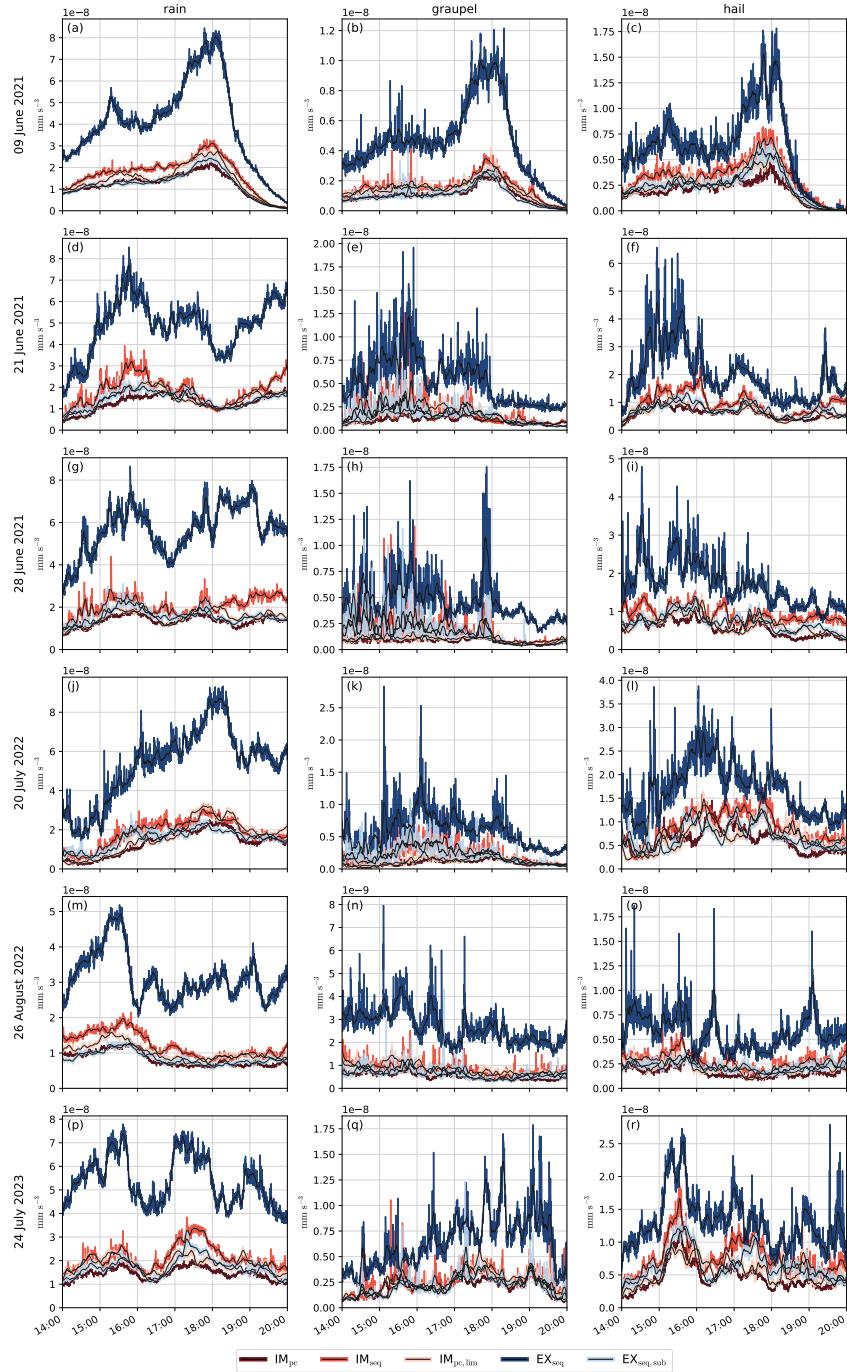
Figure B1. Time series of precipitation rate roughness, Eq. (27), for all six cases.

Author contributions. NO conceived the study idea. SB adapted the model code for idealized experiments and carried out the simulations and analysis with guidance from NO. SB prepared the manuscript with inputs from NO.

Competing interests. The authors declare that they have no conflict of interest.

Acknowledgements. We acknowledge funding for this study by the European Union's Horizon program via project CleanCloud (Grant No. 430   101137639). This work was supported by a grant from the Swiss National Supercomputing Centre (CSCS) under project ID lp88 on Alps.

References

Ban, N., Schmidli, J., and Schär, C.: Heavy precipitation in a changing climate: Does short-term summer precipitation increase faster?, Geophysical Research Letters, 42, 1165–1172, https://doi.org/https://doi.org/10.1002/2014GL062588, 2015.

Barrett, A. I., Wellmann, C., Seifert, A., Hoose, C., Vogel, B., and Kunz, M.: One Step at a Time: How Model Time Step Significantly Affects Convection-Permitting Simulations, Journal of Advances in Modeling Earth Systems, 11, 641–658, https://doi.org/https://doi.org/10.1029/2018MS001418, 2019.

Bauer, P., Thorpe, A., and Brunet, G.: The quiet revolution of numerical weather prediction, Nature, 525, 47–55, https://doi.org/10.1038/nature14956, 2015.

Blahak, U.: Towards a better representation of high density ice particles in a state-of-the-art two-moment bulk microphysical scheme, in: Proc. 15th Int. Conf. Clouds and Precip., Cancun, Mexico, vol. 20208, 2008.

Blahak, U.: New implementation of explicit hydrometeor sedimentation in the Seifert-Beheng 2-moment bulk microphysical scheme, https://www.cosmo-model.org/content/model/documentation/core/docu_sedi_twomom.pdf, accessed: 07 May 2025, 2020.

Bolt, S. and Omanovic, N.: Data for publication "Evaluation of Semi-Implicit and Explicit Sedimentation Approaches in the Two- Moment Cloud Microphysics Scheme of ICON", https://doi.org/10.5281/zenodo.15608275, 2025a.

Bolt, S. and Omanovic, N.: Scripts for publication "Evaluation of Semi- Implicit and Explicit Sedimentation Approaches in the Two-Moment Cloud Microphysics Scheme of ICON", https://doi.org/10.5281/zenodo.15609459, 2025b.

Crameri, F., Shephard, G. E., and Heron, P. J.: The misuse of colour in science communication, Nature Communications, 11, https://doi.org/10.1038/s41467-020-19160-7, 2020.

Dai, A.: Global Precipitation and Thunderstorm Frequencies. Part II: Diurnal Variations, Journal of Climate, 14, 1112 – 1128, https://doi.org/10.1175/1520-0442(2001)014<1112:GPATFP>2.0.CO;2, 2001.

Doms, G., Förstner, J., Heise, E., Herzog, H.-J., Mironov, D., Raschendorfer, M., Reinhardt, T., Ritter, B., Schrodin, R., Schulz, J.-P., and Vogel, G.: COSMO-Model Version 6.00: A Description of the Nonhydrostatic Regional COSMO-Model - Part II: Physical Parametrizations, https://doi.org/10.5676/DWD_PUB/NWV/COSMO-DOC_6.00_II, 2021.

Feldmann, M., Germann, U., Gabella, M., and Berne, A.: A characterisation of Alpine mesocyclone occurrence, Weather and Climate Dynamics, 2, 1225–1244, https://doi.org/10.5194/wcd-2-1225-2021, 2021.

Fuhrer, O., Osuna, C., Lapillonne, X., Gysi, T., Cumming, B., Bianco, M., Arteaga, A., and Schulthess, T. C.: Towards a performance portable, architecture agnostic implementation strategy for weather and climate models, Supercomputing Frontiers and Innovations, 1, 45–62, https://doi.org/10.14529/jsfi140103, 2014.

Fuhrer, O., Chadha, T., Hoefler, T., Kwasniewski, G., Lapillonne, X., Leutwyler, D., Lüthi, D., Osuna, C., Schär, C., Schulthess, T. C., and Vogt, H.: Near-global climate simulation at 1 km resolution: establishing a performance baseline on 4888 GPUs with COSMO 5.0, Geoscientific Model Development, 11, 1665–1681, https://doi.org/10.5194/gmd-11-1665-2018, 2018.

Heim, C., Panosetti, D., Schlemmer, L., Leuenberger, D., and Schär, C.: The Influence of the Resolution of Orography on the Simulation of Orographic Moist Convection, Monthly Weather Review, 148, 2391 – 2410, https://doi.org/10.1175/MWR-D-19-0247.1, 2020.

Heinze, R., Dipankar, A., Henken, C. C., Moseley, C., Sourdeval, O., Trömel, S., Xie, X., Adamidis, P., Ament, F., Baars, H., Barthlott, C., Behrendt, A., Blahak, U., Bley, S., Brdar, S., Brueck, M., Crewell, S., Deneke, H., Di Girolamo, P., Evaristo, R., Fischer, J., Frank, C., Friederichs, P., Göcke, T., Gorges, K., Hande, L., Hanke, M., Hansen, A., Hege, H.-C., Hoose, C., Jahns, T., Kalthoff, N., Klocke, D., Kneifel, S., Knippertz, P., Kuhn, A., van Laar, T., Macke, A., Maurer, V., Mayer, B., Meyer, C. I., Muppa, S. K.,

Neggers, R. A. J., Orlandi, E., Pantillon, F., Pospichal, B., Röber, N., Scheck, L., Seifert, A., Seifert, P., Senf, F., Siligam, P., Simmer, C., Steinke, S., Stevens, B., Wapler, K., Weniger, M., Wulfmeyer, V., Zängl, G., Zhang, D., and Quaas, J.: Large-eddy simulations over Germany using ICON: a comprehensive evaluation, Quarterly Journal of the Royal Meteorological Society, 143, 69–100, https://doi.org/https://doi.org/10.1002/qj.2947, 2017.

ICON partnership (MPI-M, DWD, DKRZ, KIT, and C2SM): ICON release 2024.10, https://doi.org/10.35089/WDCC/IconRelease2024.10, 2024.

Kendon, E. J., Roberts, N. M., Fowler, H. J., Roberts, M. J., Chan, S. C., and Senior, C. A.: Heavier summer downpours with climate change revealed by weather forecast resolution model, Nature Climate Change, 4, 570–576, https://doi.org/10.1038/nclimate2258, 2014.

Lean, H. W., Clark, P. A., Dixon, M., Roberts, N. M., Fitch, A., Forbes, R., and Halliwell, C.: Characteristics of High-Resolution Versions of the Met Office Unified Model for Forecasting Convection over the United Kingdom, Monthly Weather Review, 136, 3408 – 3424, https://doi.org/10.1175/2008MWR2332.1, 2008.

Leutwyler, D., Fuhrer, O., Lapillonne, X., Lüthi, D., and Schär, C.: Towards European-scale convection-resolving climate simulations with GPUs: a study with COSMO 4.19, Geoscientific Model Development, 9, 3393–3412, https://doi.org/10.5194/gmd-9-3393-2016, 2016.

Mansell, E. R.: On Sedimentation and Advection in Multimoment Bulk Microphysics, Journal of the Atmospheric Sciences, 67, 3084 – 3094, https://doi.org/10.1175/2010JAS3341.1, 2010.

Mikkola, J., Sinclair, V. A., Bister, M., and Bianchi, F.: Daytime along-valley winds in the Himalayas as simulated by the Weather Research and Forecasting (WRF) model, Atmospheric Chemistry and Physics, 23, 821–842, https://doi.org/10.5194/acp-23-821-2023, 2023.

Milbrandt, J. A. and Yau, M. K.: A Multimoment Bulk Microphysics Parameterization. Part I: Analysis of the Role of the Spectral Shape Parameter, Journal of the Atmospheric Sciences, 62, 3051 – 3064, https://doi.org/10.1175/JAS3534.1, 2005.

Miyamoto, Y., Kajikawa, Y., Yoshida, R., Yamaura, T., Yashiro, H., and Tomita, H.: Deep moist atmospheric convection in a subkilometer global simulation, Geophysical Research Letters, 40, 4922–4926, https://doi.org/https://doi.org/10.1002/grl.50944, 2013.

Noppel, H., Blahak, U., Seifert, A., and Beheng, K. D.: Simulations of a hailstorm and the impact of CCN using an advanced two-moment cloud microphysical scheme, Atmospheric Research, 96, 286–301, https://doi.org/https://doi.org/10.1016/j.atmosres.2009.09.008, 15th International Conference on Clouds and Precipitation, 2010.

Omanovic, N., Goger, B., and Lohmann, U.: The impact of the mesh size and microphysics scheme on the representation of mid-level clouds in the ICON model in hilly and complex terrain, Atmospheric Chemistry and Physics, 24, 14 145–14 175, https://doi.org/10.5194/acp-24-14145-2024, 2024.

Owens, J. D., Houston, M., Luebke, D., Green, S., Stone, J. E., and Phillips, J. C.: GPU Computing, Proceedings of the IEEE, 96, 879–899, https://doi.org/10.1109/JPROC.2008.917757, 2008.

Paredes, E. G., Groner, L., Ubbiali, S., Vogt, H., Madonna, A., Mariotti, K., Cruz, F., Benedicic, L., Bianco, M., VandeVondele, J., and Schulthess, T. C.: GT4Py: High Performance Stencils for Weather and Climate Applications using Python, https://arxiv.org/abs/2311.08322, 2023.

Project ICON-22: ICON-22 - MeteoSwiss, https://www.meteoswiss.admin.ch/about-us/research-and-cooperation/projects/2023/icon-22.html, accessed: 07 May 2025, 2025.

Reinert, D., Rieger, D., and Prill, F.: ICON Tutorial 2024: Working with the ICON Model, https://doi.org/10.5676/DWD_PUB/NWV/ICON_TUTORIAL2024, 2024.

Reinert, D., Prill, F., Frank, H., Denhard, M., Baldauf, M., Schraff, C., Gebhardt, C., Marsigli, C., Förstner, J., Zängl, G., Schlemmer, L., Blahak, U., and Welzbacher, C.: DWD Database Reference for the Global and Regional ICON and ICON-EPS Forecasting System, https://

10.5194/egusphere-2025-2804
2025-06-26
Author(s) 2025. CC BY 4.0 License.

www.dwd.de/SharedDocs/downloads/DE/modelldokumentationen/nwv/icon/icon_dbbeschr_aktuell.pdf, version 2.5.0, accessed: 07 May 2025, 2025.

Schmidli, J., Böing, S., and Fuhrer, O.: Accuracy of Simulated Diurnal Valley Winds in the Swiss Alps: Influence of Grid Resolution, Topography Filtering, and Land Surface Datasets, Atmosphere, 9, https://doi.org/10.3390/atmos9050196, 2018.

Segal, Y. and Khain, A.: Dependence of droplet concentration on aerosol conditions in different cloud types: Application to droplet concentration parameterization of aerosol conditions, Journal of Geophysical Research: Atmospheres, 111, https://doi.org/https://doi.org/10.1029/2005JD006561, 2006.

Seifert, A.: On the Parameterization of Evaporation of Raindrops as Simulated by a One-Dimensional Rainshaft Model, Journal of the Atmospheric Sciences, 65, 3608 – 3619, https://doi.org/10.1175/2008JAS2586.1, 2008.

Seifert, A. and Beheng, K. D.: A two-moment cloud microphysics parameterization for mixed-phase clouds. Part 1: Model description, Meteorology and Atmospheric Physics, 92, 45–66, https://doi.org/10.1007/s00703-005-0112-4, 2006.

Seifert, A., Blahak, U., and Buhr, R.: On the analytic approximation of bulk collision rates of non-spherical hydrometeors, Geoscientific Model Development, 7, 463–478, https://doi.org/10.5194/gmd-7-463-2014, 2014.

Skamarock, W. C.: Positive-Definite and Monotonic Limiters for Unrestricted-Time-Step Transport Schemes, Monthly Weather Review, 134, 2241 – 2250, https://doi.org/10.1175/MWR3170.1, 2006.

Smolarkiewicz, P. K. and Pudykiewicz, J. A.: A Class of Semi-Lagrangian Approximations for Fluids, Journal of Atmospheric Sciences, 49, 2082 – 2096, https://doi.org/10.1175/1520-0469(1992)049<2082:ACOSLA>2.0.CO;2, 1992.

Staniforth, A. and Côté, J.: Semi-Lagrangian Integration Schemes for Atmospheric Models—A Review, Monthly Weather Review, 119, 2206 – 2223, https://doi.org/10.1175/1520-0493(1991)119<2206:SLISFA>2.0.CO;2, 1991.

Stevens, B., Acquistapace, C., Hansen, A., Heinze, R., Klinger, C., Klocke, D., Rybka, H., Schubotz, W., Windmiller, J., Adamidis, P., Arka, I., Barlakas, V., Biercamp, J., Brueck, M., Brune, S., Buehler, S. A., Burkhardt, U., Cioni, G., Costa-Surós, M., Crewell, S., Crüger, T., Deneke, H., Friederichs, P., Henken, C. C., Hohenegger, C., Jacob, M., Jakub, F., Kalthoff, N., Köhler, M., van Laar, T. W., Li, P., Löhnert, U., Macke, A., Madenach, N., Mayer, B., Nam, C., Naumann, A. K., Peters, K., Poll, S., Quaas, J., Röber, N., Rochetin, N., Scheck, L., Schemann, V., Schnitt, S., Seifert, A., Senf, F., Shapkalijevski, M., Simmer, C., Singh, S., Sourdeval, O., Spickermann, D., Strandgren, J., Tessiot, O., Vercauteren, N., Vial, J., Voigt, A., and Zängl, G.: The Added Value of Large-eddy and Storm-resolving Models for Simulating Clouds and Precipitation, Journal of the Meteorological Society of Japan. Ser. II, 98, 395–435, https://doi.org/10.2151/jmsj.2020-021, 2020.

Wacker, U. and Seifert, A.: Evolution of rain water profiles resulting from pure sedimentation: Spectral vs. parameterized description, Atmospheric Research, 58, 19–39, https://doi.org/https://doi.org/10.1016/S0169-8095(01)00081-3, 2001.

Zängl, G., Reinert, D., Rípodas, P., and Baldauf, M.: The ICON (ICOsahedral Non-hydrostatic) modelling framework of DWD and MPI-M: Description of the non-hydrostatic dynamical core, Quarterly Journal of the Royal Meteorological Society, 141, 563–579, https://doi.org/https://doi.org/10.1002/qj.2378, 2015.